

# The Earth's mantle in a microwave oven: thermal convection driven by a heterogeneous distribution of heat sources

Loïc Fourel<sup>1</sup> · Angela Limare<sup>1</sup> · Claude Jaupart<sup>1</sup> · Emanoil Surducan<sup>2</sup> ·  
Cinzia G. Farnetani<sup>1</sup> · Edouard C. Kaminski<sup>1</sup> · Camelia Neamtu<sup>2</sup> · Vasile Surducan<sup>2</sup>

Received: 22 February 2017 / Revised: 14 May 2017 / Accepted: 8 June 2017  
© Springer-Verlag GmbH Germany 2017

**Abstract** Convective motions in silicate planets are largely driven by internal heat sources and secular cooling. The exact amount and distribution of heat sources in the Earth are poorly constrained and the latter is likely to change with time due to mixing and to the deformation of boundaries that separate different reservoirs. To improve our understanding of planetary-scale convection in these conditions, we have designed a new laboratory setup allowing a large range of heat source distributions. We illustrate the potential of our new technique with a study of an initially stratified fluid involving two layers with different physical properties and internal heat production rates. A modified microwave oven is used to generate a uniform radiation propagating through the fluids. Experimental fluids are solutions of hydroxyethyl cellulose and salt in water, such that salt increases both the density and the volumetric heating rate. We determine temperature and composition fields in 3D with non-invasive techniques. Two fluorescent dyes are used to determine temperature. A Nd:YAG planar laser beam excites fluorescence, and an optical system, involving a beam splitter and a set of colour filters, captures the fluorescence intensity distribution on two separate spectral bands. The ratio between the two intensities provides an instantaneous determination of temperature with an uncertainty of 5% (typically 1K). We quantify mixing processes by precisely tracking the interfaces separating the two

fluids. These novel techniques allow new insights on the generation, morphology and evolution of large-scale heterogeneities in the Earth's lower mantle.

## 1 Introduction

Convection in the Earth's mantle, which is responsible for plate tectonics and the secular cooling of our planet, is largely driven by internal heat generation due to the decay of long-lived isotopes of uranium, thorium and potassium, with a contribution from the Earth's core that remains poorly constrained (Jaupart et al. 2015). The existence of two apparently independent scales of motion, a large-scale one that is associated with sea floor spreading and subduction and another one involving isolated upwellings that feed intraplate volcanoes called "hotspots", has been explained by instabilities of two boundary layers at the top and at the base of the mantle. In this framework, the heat flux carried by hotspots is equal to heat supply from the Earth's core. This is not consistent with current estimates, however (Jaupart et al. 2015), which has been explained in various ways. It is quite likely that the formation of the core and the giant meteorite impact that generated the Moon soon after the planet accretion left a heterogeneous mantle (Kaminski and Javoy 2013). Furthermore, an early stratified mantle may have been modified by the extraction of continental material and by convective mixing. The anomalous isotopic composition of hotspot lavas supports the existence of deep mantle heterogeneities (Hofmann 1997) and has been linked to primordial mantle material by some authors (Moreira et al. 2001; Boyet and Carlson 2005; Labrosse et al. 2007). Regardless of its origin, this material must have larger concentrations of radioactive elements than the upper mantle (McDonough and Sun 1995; Kellogg et al.

✉ Loïc Fourel  
fourel@ipggp.fr

<sup>1</sup> Institut de Physique du Globe de Paris, 1 Rue Jussieu,  
75238 Paris Cedex 05, France

<sup>2</sup> National Institute for Research and Development  
of Isotopic and Molecular Technologies, 67-103 Donath St.,  
400293 Cluj-Napoca, Romania

1999; Javoy and Kaminski 2014; Arevalo et al. 2013). A lower mantle layer with enhanced heat production is likely to generate motions that can be interpreted as due to heat supplied by the Earth's core. These fundamental issues have motivated research on the characteristics and physical properties of the lower mantle close to the core-mantle boundary (CMB). There, high-resolution seismological studies have revealed the existence of two broad regions beneath Africa and the Pacific with anomalously low shear-wave velocity called LLSVPs (for large low shear velocity provinces) (Dziewonski 1984; Wen et al. 2001; Lekic et al. 2012; Cottaar and Lekic 2016). LLSVPs have sharp edges that appear to be located below hotspots and seem stable over hundreds of million years (Torsvik et al. 2008; Garnero et al. 2016).

Current limitations on the resolution of seismic tomography methods do not allow discrimination between compositional and purely thermal origins for LLSVPs (Masters et al. 2000; Tackley 2002; Davies et al. 2015; Garnero et al. 2016). If one appeals to the former origin, one must assess how a compositionally stratified mantle evolves in the presence of convective motions. One can anticipate that these motions act to deform the boundaries of chemically distinctive domains and induce mixing. One must, therefore, also determine which conditions allow the long-term survival of primordial material at the base of the mantle. Answers to these questions depend on a host of variables and parameters that remain poorly constrained for the Earth's mantle, such as the intrinsic density and heat production differences between the basal material and the mantle above. An alternative strategy is to focus on the shapes of LLSVPs and on their apparent lack of mobility for hundreds of million years. So far, this problem has been tackled mainly by numerical calculations (Tackley 2002; Nakagawa and Tackley 2014; Deschamps and Tackley 2008, 2009). These calculations, however, suffer from limitations on the accuracy of mixing processes, especially in 3-D (van Keken et al. 1997; Davies et al. 2007; Leng and Zhong 2011). Mixing phenomena can be studied in the laboratory but, so far, all studies have been carried out in a Rayleigh-Bénard configuration with no internal heating (Davaille 1999; Gonnermann et al. 2002; Jellinek and Manga 2002; Le Bars and Davaille 2002). This has motivated us to develop a flexible experimental method allowing the tracking of deformation and mixing in heterogeneous convective systems driven by internal heat sources.

Very few laboratory experiments of internally heated convection are available owing to difficulties in controlling the distribution of heat sources in a large volume. Previous studies have been focussed mostly on the planform of convection in ionized aqueous solutions (Tritton and Zarraga 1967; Schwiderski and Schwab 1971; Kulacki and Goldstein 1972; Kulacki and Nagle 1975; Tasaka et al. 2005;

Takahashi et al. 2010). Limare et al. (2015) used a new experimental apparatus based on microwave (MW) absorption and explored a wide range of dynamical regimes in highly viscous fluids. We have improved this setup to deal with a stratified system involving two fluids with different intrinsic densities and heat production rates. The main challenge was to track both composition and temperature. Common techniques rely on fluorescent tracers for composition and thermocouples or thermochromic liquid crystals for temperature (Limare et al. 2015), but they are not appropriate for our microwave setup. One cannot introduce metal compounds in a MW oven, which rules out thermocouples. In addition, thermochromic liquid crystals do not allow the accurate visualization of isotherms in the presence of fluorescent tracers. We have, therefore, developed a laser-induced fluorescence (LIF) technique to monitor temperature and composition simultaneously. LIF has already been used successfully in a few experimental studies (Bruchhausen et al. 2005; Funatani et al. 2004; Sakakibara and Adrian 1999; Hishida and Sakakibara 2000; Sakakibara and Adrian 2004).

This paper is divided into three main parts. Section 2 deals with details of our experimental setup. Section 3 describes our methods to monitor temperature and composition in a fluid. A final part is devoted to one particular experiment on convection driven by internal heating in an initially layered system (Sects. 4, 5).

## 2 Experimental setup

Photographs of the experimental setup are shown in Fig. 1. A highly modified microwave oven is fixed to an optical table to guarantee the stability of the optical paths. A power generator driven by an embedded control system and a specifically designed MW radiation waveguide lead to a stable and homogeneous source of radiation in the working fluids (Surducun et al. 2014).

The  $30 \times 30 \text{ cm}^2$  wide and 5 cm high tank is made of 30 mm thick poly(methyl-methacrylate) walls that allow good thermal insulation and are transparent to visible light and MW radiation. The bottom and side boundaries are rigid and can be considered as adiabatic, whereas the top boundary is rigid and isothermal; its temperature is set by an aluminum heat exchanger where thermostated water is circulated. We took special care to achieve a constant and uniform temperature at the upper boundary. A type-K thermocouple records the temperature inside the top aluminum plate every 5 s. Following a short transient initial phase, this temperature varies by less than  $0.1 \text{ }^\circ\text{C}$  in both space and time, which is a very small fraction of the overall temperature difference across the fluid layers (typically  $20\text{--}35 \text{ }^\circ\text{C}$ ).

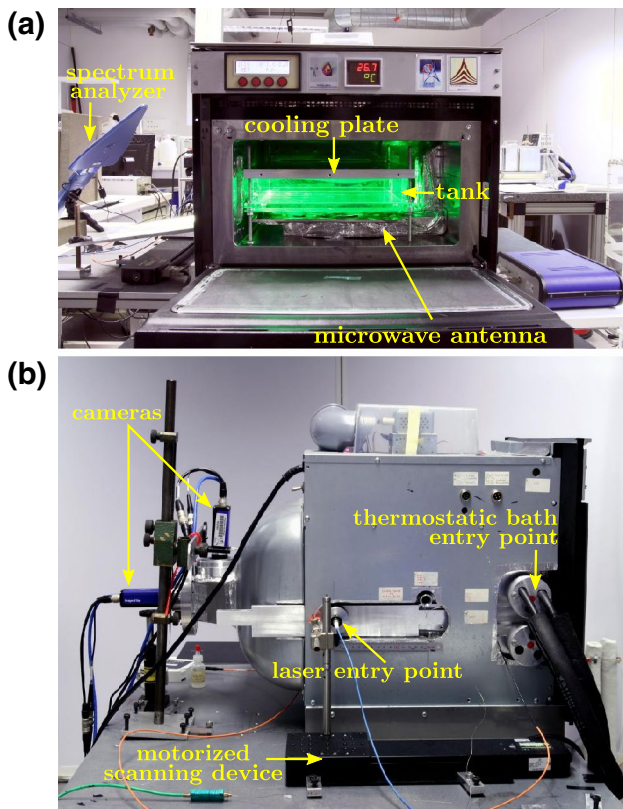


**Fig. 1** Photographs of the experimental apparatus: **a** front view, **b** side view

Experimental fluids are transparent aqueous solutions of hydroxyethyl cellulose (also called Natrosol) whose viscosities vary within a large range depending on concentration. We measured their physical properties in the laboratory as a function of temperature (examples are given in Sect. 4). Viscosity is measured with a Thermo Scientific Haake rheometer RS600, and the equation of state is determined with a DMA 5000 Anton Paar densimeter (Limare et al. 2013). Thermal diffusivity is measured by the photopyroelectric method (Dadarlat and Neamtu 2009).

MW attenuation in the experimental fluids depends on dielectric properties that are measured using an Agilent N5230A vector network analyzer and an 85070E performance dielectric probe kit (Surducan et al. 2012). It is worth noting that, at the oven magnetron operating frequency (2.47 GHz) and at a temperature of 23 °C, the dielectric properties of Natrosol solutions (with concentrations of up to 1 wt%) and distilled water are almost identical. Adding sodium chloride salt to these solutions acts to increase both density and MW absorption. We were thus able to achieve a stratified system with perfectly miscible fluids. Viscosities of our experimental fluids were large enough for inertia to be negligible, matching conditions

in the Earth's mantle (Davaille and Limare 2015). These solutions are coloured with fluorescent dyes in order to measure temperature via ratiometric LIF (see Sect. 3.1). Using different dye concentrations in the two experimental fluids, we are able to track their interface. A Nd:Yag laser ( $\lambda_{\text{ex}} = 532 \text{ nm}$ ) coupled via an optical fiber to a 2-D beam expander is mounted on a microprocessor-controlled scanning device that sweeps through half of the tank in the  $y$ -direction with submillimetric accuracy. The emitted light is divided by a beam splitter and registered by two (CCD) E-lite cameras (1.4 Mpixels, 17 Hz) from LaVision with a resolution of 5 pixels per millimeter. Correspondence of their images is achieved by careful calibration and stereo matching algorithms from LaVision. Each camera is equipped with different colour filters (see Sect. 3.3). A MW filter was specially designed in order to protect the cameras' high sensitivity CCD sensor as well as the operator from MW radiation (Surducan and Surducan 2014). MW leakage from the oven was continuously monitored with a spectrum analyzer Spectran HF 4060 from Aaronia Corp.

Inside the oven, the microwaves propagate in a down/up-down manner. The incidence surface is located at the bottom of the tank (Fig. 1a). Therefore, the microwaves are first absorbed by the lower layer and then by the upper layer. The transmitted part is then reflected by the metallic heat exchanger and propagates back into the top and bottom layer, respectively. After such a round trip through the two working fluids, less than 0.25% of the incident radiation is sent back to the MW guide.

Each experiment followed the same protocol. The tank was first completely filled with the lighter fluid and air bubbles were carefully eliminated. The tank was then placed into the oven to make reference images at a series of fixed locations in the  $y$  direction. Next, a known volume of denser fluid was injected at the base of the tank forcing the excess lighter fluid out. The dense fluid was allowed to spread across the whole lower boundary before new reference images were taken at the same  $y$  locations as before and at room temperature. Thermostated water at room temperature was then allowed to flow through the top aluminium plate and the oven was turned on at a prescribed power. Images were taken on both cameras simultaneously as the tank was scanned repeatedly.

### 3 Optical assembly and fluorescent dyes

The optical system, which is an important part of the experiment, is shown schematically in Fig. 2 and described further in this section. We first explain the principles of ratiometric LIF before going into the detailed properties of the fluorescent dyes and the colour filters.

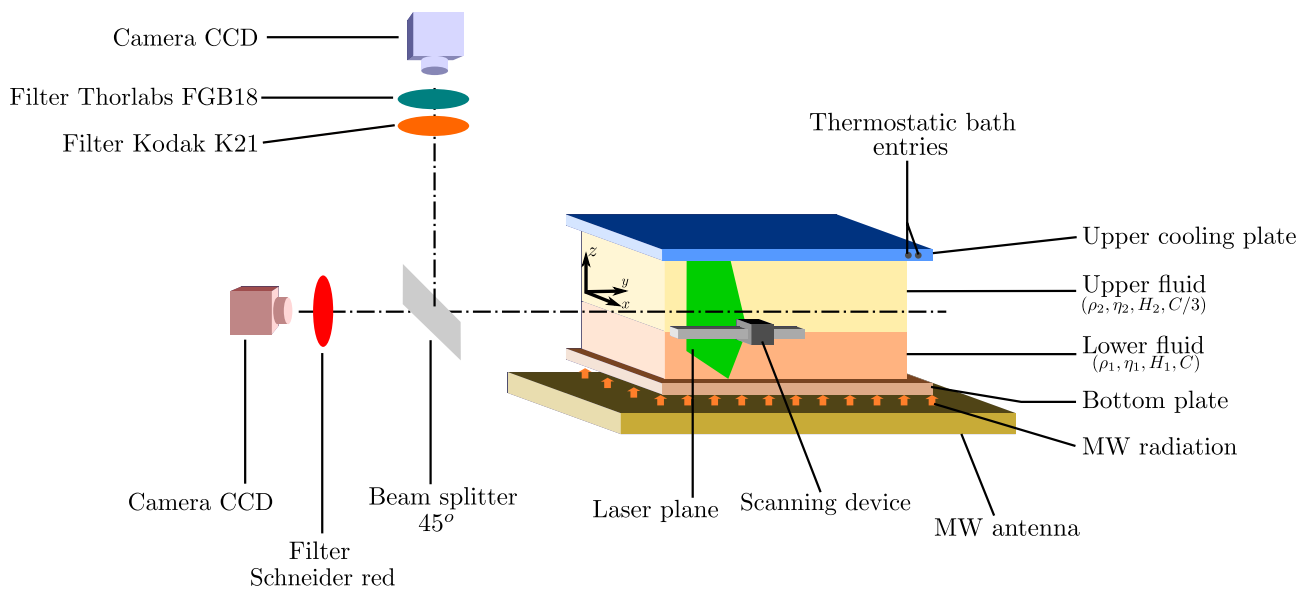


**Fig. 2** Experimental and optical setup. Dyes concentrations are three times higher in the lower fluid than in the upper one. Two CCD cameras record the fluorescence intensity of dye tracers in two different

spectral bands that are isolated from the full spectrum by two different sets of colour filters (see Table 1 for filters characteristics and Table 2 for variables definition)

### 3.1 Brief review of two-colour laser-induced fluorescence

Fluorescence intensity,  $I_f$ , is related to temperature as follows (Lemoine et al. 1999):

$$I_f = K_{\text{opt}} K_{\text{spec}} V_c I_0 C e^{\beta_f/T}, \quad (1)$$

where  $K_{\text{opt}}$  is an optical constant,  $K_{\text{spec}}$  is another constant which depends only on the spectroscopic properties of the fluorescent tracer,  $V_c$  is the fluorescence collection volume,  $I_0$  is the laser excitation intensity,  $C$  stands for the molecular tracer concentration,  $T$  is temperature and  $\beta_f$  characterizes the temperature dependence of the dye tracer. Determining temperature from a single dye and single colour technique is associated with several difficulties. The main one, which is of special relevance to the present study, is that the dye response does not depend on temperature only and varies with the laser intensity,  $I_0$ , which may change with time due to changing conditions in the laboratory or due to the development of instabilities within the tank. This difficulty can be overcome with two dyes having different fluorescence responses (Sakakibara and Adrian 1999, 2004; Hishida and Sakakibara 2000; Bruchhausen et al. 2005). The fluorescence signals of the two dyes lie in two different spectral bands and can be measured simultaneously. Following equation (1), the ratio between the two intensities  $I_{f1}$  and  $I_{f2}$  is:

$$R_f(T) = \frac{I_{f1}}{I_{f2}} = \frac{K_{\text{opt}1} K_{\text{spec}1} C_1}{K_{\text{opt}2} K_{\text{spec}2} C_2} e^{\frac{\beta_1 - \beta_2}{T}}, \quad (2)$$

where the various constants have been labelled 1 and 2 depending on the dye. The exponential prefactor in this equation is constant for a given combination of dye tracers, fluids, detection system, excitation wavelength and spectral bands. One further simplification is to use a reference measurement at a known temperature,  $T_0$ , such that:

$$\ln \left( \frac{R_f(T)}{R_f(T_0)} \right) = \beta \left( \frac{1}{T} - \frac{1}{T_0} \right). \quad (3)$$

Parameter  $\beta$  ( $= \beta_1 - \beta_2$ ) is determined with a careful calibration procedure (see Sect. 3.4).

### 3.2 Colour dyes and temperature sensitivity

Sutton et al. (2008) have shown that an enhanced sensitivity to temperature can be obtained with an appropriate pair of fluorescent dyes that are positively and negatively sensitive to temperature (intensity increasing or decreasing with increasing temperature), respectively. Another requirement is that the two intensity peaks must be in two well-separated wavelength bands so that each one can be filtered out with no loss of the other one. In that respect, fluorescein 27 (FL) and pyridine 1 (LDS) are suitable candidates. Originally in the form of tiny crystals or needles powders, both dyes are first dissolved within isopropanol to ensure good solubility. We then add such a small amount of these dilutions to the working fluids that their rheological properties remain unchanged. The fluorescent intensities of these dyes both vary significantly

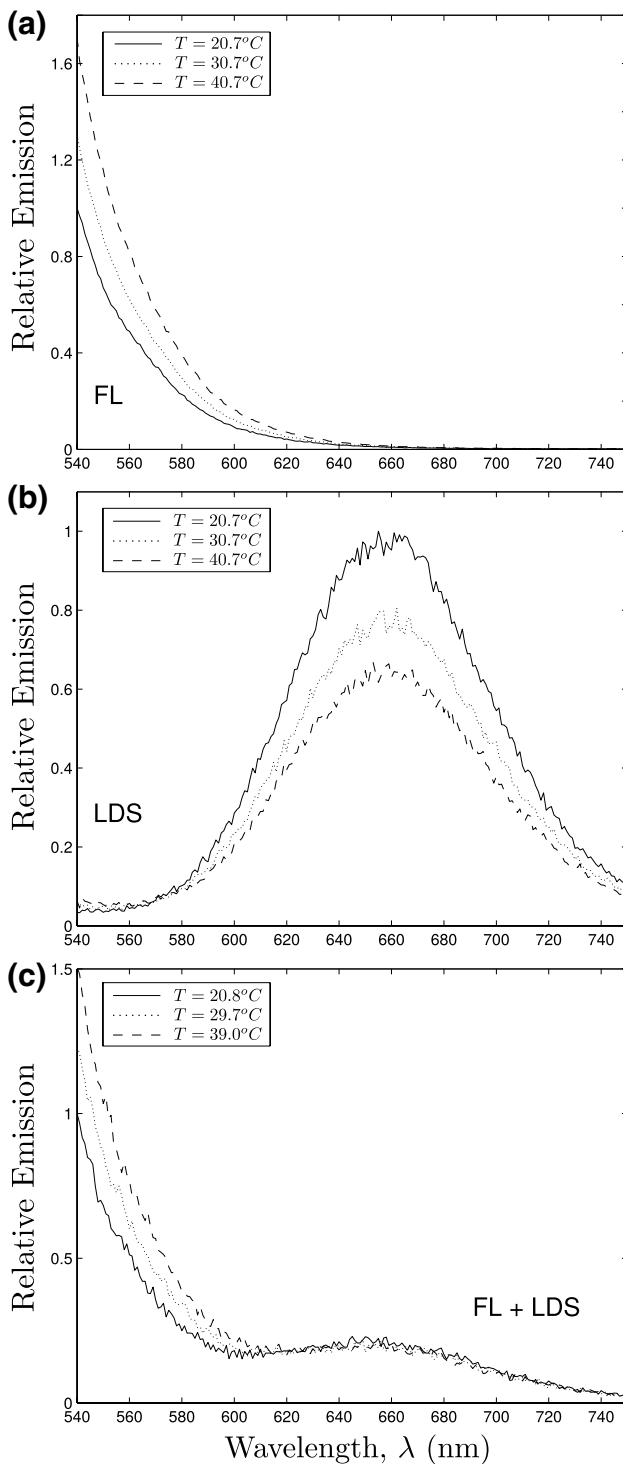


**Fig. 3** Variation of fluorescence intensity with temperature as a function of wavelength for different solutions. **a** FL in a Natrosol solution (0.3 wt%) with a concentration of  $10^{-5}$  mol L $^{-1}$ . **b** LDS in a Natrosol (0.3 wt%) solution with a concentration of  $10^{-4}$  mol L $^{-1}$ . **c** Mixture of FL and LDS in a Natrosol sample (0.3 wt%) with concentrations of  $1.5 \times 10^{-6}$  mol L $^{-1}$  and  $1.5 \times 10^{-5}$  mol L $^{-1}$ , respectively. All values are scaled to the maximum value taken by the fluorescence intensity at the lowest temperature

with temperature. The FL signal increases with increasing temperature with a peak value close to the laser excitation wavelength, as shown in Fig. 3a for a Natrosol mixture. In contrast, the LDS signal decreases with temperature with a maximum peak close to 660 nm for the same Natrosol mixture (Fig. 3b). The LDS signal is much lower than the FL one and a higher concentration of LDS is required to detect the two signals with the same accuracy. Figure 3c shows the fluorescence intensity signal in a solution with  $C_{FL} = 1.5 \times 10^{-6}$  mol L $^{-1}$  and  $C_{LDS} = 1.5 \times 10^{-5}$  mol L $^{-1}$ . The addition of the two emissions leads to an increase of fluorescence intensity with temperature at wavelengths shorter than 600 nm but the two even out at larger wavelengths, such that the bulk intensity remains nearly constant with temperature. These results are obtained with a spectrofluorometer (Fluoromax-4 from Horiba Scientific) on small samples with typical dimensions of 1 cm. In the tank, the emitted light may travel through as much as 15 cm distance before reaching the cameras, and we must, therefore, deal with dye concentrations that are small enough for re-absorption to be negligible. As shown in Sect. 3.4, a good combination is  $C_{FL} = 10^{-7}$  mol L $^{-1}$  and  $C_{LDS} = 10^{-6}$  mol L $^{-1}$  for the lower layer and 3 times less for the upper one.

### 3.3 Selection of spectral bands and colour filters

Given the fluorescence characteristics of FL and LDS (Fig. 3c), the best spectral bands are  $\lambda_1 = [540:600]$  nm and  $\lambda_2 > 620$  nm. An important constraint arises from our imaging system: the cameras are equipped with short focal length wide-angle lenses in order to capture the entire width of the tank from the short distance imposed by the oven apertures. This prevents the use of interferometric filters with sharp cut-off wavelengths because they are highly sensitive to the incidence angle. The only alternative is to use a combination of colour filters with smoother transfer functions and no sensitivity to the incidence angle. A supplementary constraint is to filter out the laser excitation wavelength on both spectral discrimination ranges. As a result, the first spectral band is isolated using Kodak filter n°21 and Thorlabs filter FGB18. For the open-ended second spectral band, we rely on a red filter from Schneider optics. Technical characteristics are listed in Table 1. Transmittance data were measured

**Table 1** Colour filter characteristics and brand denomination

Name	Brand	Characteristics (at 20% transmission)
K21	Kodak Orange Filter	High-pass $\lambda > 549$ nm
FGB18	Thorlabs	Pass band $\lambda = [355 - 607]$ nm
090 MRC	Schneider-Kreuznach	High-pass $\lambda > 592$ nm

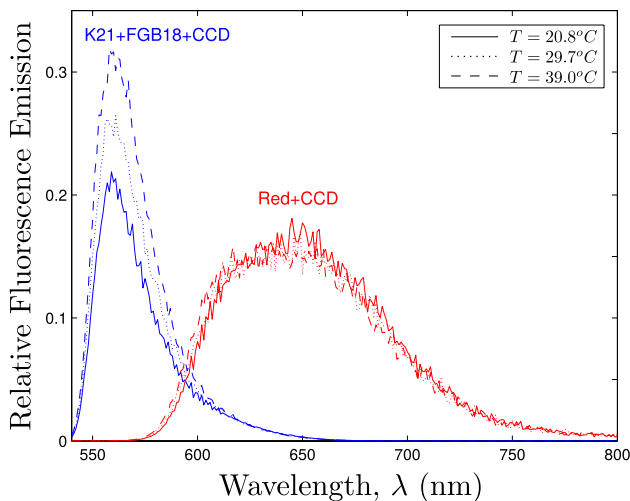


**Fig. 4** Variation of the fluorescence intensity with temperature on the two different spectral bands. The *blue* spectral band is made of filters K21, FGB18 and the corresponding CCD camera response whereas the *red* spectral band is made of filter Red and the corresponding CCD camera response. The fluorescence intensity increases with temperature in the *blue* spectral band and remains nearly constant in the *red* one

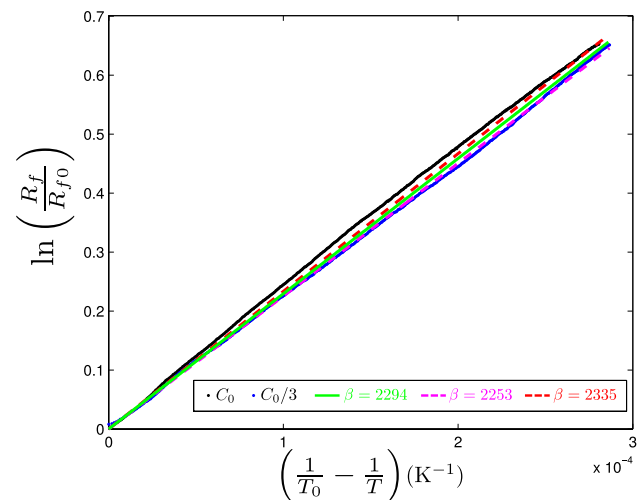
in the lab on a spectrophotometer (Evolution 600 UV–Vis from Thermo Fisher Scientific).

Figure 4 shows the predicted emission signal in each spectral band for a Natrosol solution (0.3 wt%) coloured with both dyes. It is obtained by convoluting the emission spectrum shown in Fig. 3c with each filter transfer function and camera response. One should note the positive correlation between fluorescence intensity and temperature on band 1 and the lack of such correlation in band 2. Following Sutton et al. (2008), the temperature dependence is determined from the ratio of the integrated blue and red curves in Fig. 4. We obtained a value of 2.7% per °C over the 20–40 °C temperature range, which is higher by a factor of three than that of Bruchhausen et al. (2005) (−0.8% per °C) for Rhodamine B only. It is also higher than those of Hishida and Sakakibara (2000) (−1.82% per °C) and Sakakibara and Adrian (1999) (−1.95% per °C), who used Rhodamine B and Rhodamine 101. Our result is close to that of Coppeta and Rogers (1998) (2.43% per °C) for FL alone and slightly less than that of Sutton et al. (2008) (3.5% per °C) for the same dye. Sutton et al. (2008) were able to enhance the sensitivity of FL by adding Rhodamine B or Kiton Red and obtained values up to 7% per °C. Such values are out of our reach because we cannot use interferometric filters. Our optical conditions are the best we can achieve with the laser, the filters and the optical pathlengths imposed by the experimental conditions.

### 3.4 Calibration

We calibrated the dyes sensitivities to temperature using the MW oven. The tank was filled to the two thirds with a low viscosity solution of Natrosol (0.3 wt%) coloured by FL ( $C_{FL} = 10^{-7}$  mol L $^{-1}$ ) and LDS ( $C_{LDS} = 10^{-6}$  mol L $^{-1}$ ) and placed inside the oven. An optical fiber sensor immune to electromagnetic radiation (PRB-MR1-02M-ST-L from Osensa) was placed inside the tank to monitor temperature. Power was turned on at  $\sim 150$  W with the fluid in direct contact with air at room temperature. In this low viscosity fluid, convection was vigorous and cooling by the air layer was not efficient enough to evacuate the heat generated by MW absorption. As a consequence, the fluid was well mixed and its temperature increased steadily according to a power law in time. We divided the fluorescence intensity images taken in both spectral bands at  $y = 0.1$  m to obtain the intensity ratio. This ratio was then averaged in the central region of interest over more than 300,000 measurements points (images have a resolution of  $1400 \times 230$  pixels) ensuring good statistical convergence. We repeated the same calibration procedure for lower dye concentrations (Fig. 5).

Fluorescence values decrease slightly with decreasing dye concentration. The temperature dependence coefficient in Eq. 3 (the  $\beta$  value) is determined by a linear fit through the data. We found that  $\beta = 2253 \pm 20$  (magenta dashed line) for the low concentration fluid and  $\beta = 2335 \pm 23$



**Fig. 5** Calibration of the fluorescence intensity ratio recorded at  $y = 0.1$  m for two different fluids with different tracer concentrations. Composition  $C_0$  (black dots) corresponds to a solution with  $C_{FL} = 10^{-7}$  mol L $^{-1}$  and  $C_{LDS} = 10^{-6}$  mol L $^{-1}$ . Composition  $C_1$  (blue dots) corresponds to dye concentrations that are smaller than the previous ones by a factor of three. The red and magenta dashed lines are the best linear fits to the data for these two solutions. The chosen linear fit linking fluorescent intensity to temperature is represented by the green line

(red dashed line) for the high concentration one. The uncertainty on  $\beta$  comes from the temperature values which are determined at a single point and which may differ from volume-averaged values. The slightly different values for the two solutions may be attributed to the effect of dye concentration on emission efficiency or to a small amount of re-absorption of FL by LDS due to the overlap between the FL emission and LDS absorption spectra. We further investigate this aspect in Sect. 3.5. When mixing occurs in a two-layered experiment, it becomes difficult to differentiate between the two fluids; hence, we chose to use the same temperature dependence coefficient for the two fluids as well as for their mixture. We can make this simplification since the ratio of dyes concentrations,  $C_1/C_2$ , is the same in both fluids and therefore remains constant while mixing takes place. Thus, we took the average  $\beta$  value of 2294 (green line in Fig. 5). One consequence is that the uncertainty on temperature is increased to 5%, or typically 1 K in our experiments, which is a small fraction of the total temperature difference across the tank ( $\sim 20$  K). This is slightly better than the initial setup of Sakakibara and Adrian (1999), which had an accuracy of  $\pm 1.4$  K, and slightly worse than their later setup, which achieved a random error smaller than 0.17 K with a post-processing convolution technique (Sakakibara and Adrian 2004).

The light path from the laser sheet to the cameras changes significantly as we scan half of the tank from  $y = 0$  to  $y = 0.15$  m. We therefore took care to evaluate variations of the  $\beta$  coefficient as a function of path length by measuring the fluorescence ratio at different  $y$ -locations in the most concentrated solution. We found that the fluorescence intensity changes by less than 2%, leading to an uncertainty in the  $\beta$  value that is within the above range.

### 3.5 Spectral conflicts and quenching assessments

The use of two dyes within the working fluids in the scope of dual LIF may lead to different kinds of spectral conflicts as detailed in Coppeta and Rogers (1998). In our case, the FL and LDS emission spectra overlap (type I conflict) as seen in Fig. 4. One visible consequence is the absence of sensitivity to temperature in the red spectral band despite the fact that LDS intensity is negatively correlated with temperature. This leads to an overall loss of temperature sensitivity. But since we calibrated the fluorescent dyes in the same conditions as the convection experiment, this effect is taken care of in the derived relationship between fluorescent intensity and temperature. Another difficulty arises from the overlap of LDS absorption and FL emission spectra. Since LDS absorption does not vary significantly with temperature (Coppeta and Rogers 1998), this qualifies as a type II spectral conflict. It can lead to re-absorption of FL emission by LDS which could be source

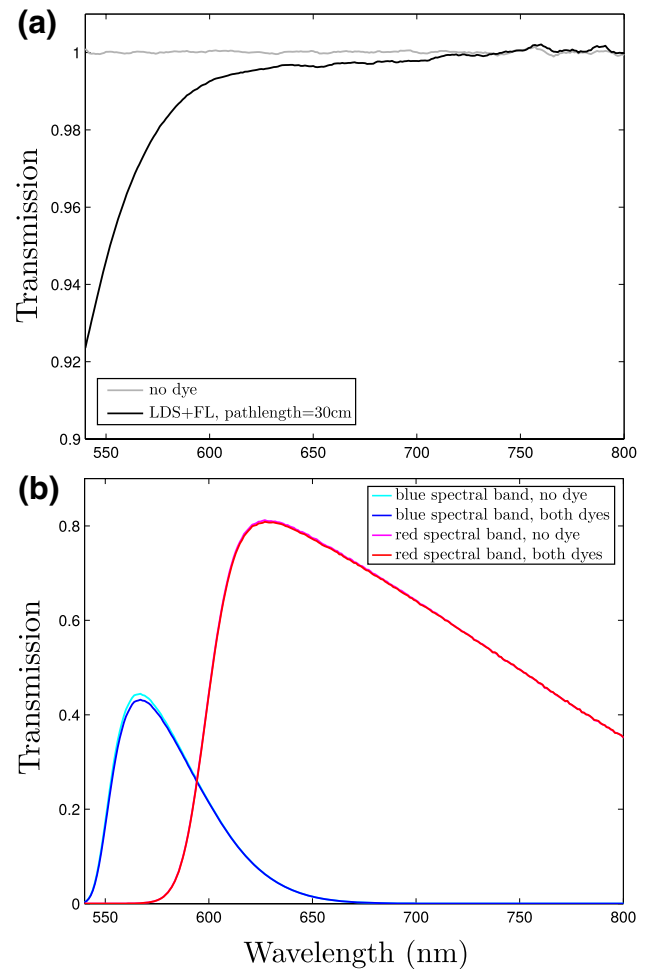


**Fig. 6** **a** Transmission spectra for a Natrosol solution with no dye (light grey line), and a Natrosol solution dyed with both FL and LDS with concentrations equivalent to a 30 cm light path (black line). **b** Transmission spectra on each camera for the same two solutions (cyan and blue lines for the blue spectral band, magenta and red lines for the red spectral band). Signal only differs by 2.1% on the blue spectral band

of errors in temperature measurements especially when the fluorescence pathlengths are large. In order to assess how this phenomenon eventually impacts our method, we have measured the absorption spectrum of our experimental fluid with a spectrophotometer using a working cell of 1 cm pathlength. To achieve the same light path as that through the experimental tank (30 cm), the Natrosol solution sample contained both dyes with a total concentration 30 times larger than the largest concentration used in the experiments. The resulting transmission spectrum is shown in Fig. 6a along with the spectrum of a Natrosol solution containing no dye for comparison. The lowest transmission (92%) takes place at the lower end of the spectrum where the LDS absorption is the highest. We calculated the total light received by each camera from the convolution of the

transmission data with the colour filters and the cameras responses. In our spectral discrimination range, the filters cut drastically the transmitted light as can be seen in Fig. 6b. Only the light received by the camera in the blue spectral band is slightly affected and the difference with respect to the spectrum of a pure Natrosol solution with no dye is only 2.1%. This small difference means that the absorption does not depend significantly on pathlength which is mainly due to the low concentrations in LDS and FL used in our experiment. It compares well with the uncertainty observed when we varied the laser sheet position in the tank during the calibration. This error contributes to the 5% error found in Sect. 3.4. Another potential source of errors due to the overlap of LDS absorption and FL emission spectra is the Förster resonant energy transfer (FRET). But a comparison of emission spectra for solutions only dyed with FL and solutions dyed with both LDS and FL showed no decrease of FL emission intensity when LDS was added. Additionally, FRET occurs if the distance between the two types of dye molecules are within a range of  $10^{-9}$  to  $10^{-8}$  m (Andrews 1989). Given the FL and LDS concentrations used in this study, the average molecular distance is about  $10^{-7}$  m, at least ten times larger than the Förster critical distance. The effect of FRET is therefore expected to be negligible. In any case, the calibration procedure was carried out in exactly the same conditions as the convection experiments, so that any potential FRET, if it did exist, was taken into account. Finally, we assessed the effect of salt (NaCl), since the presence of Cl ions could potentially favor fluorescence quenching (Geddes 2001), but its influence was found to be insignificant on fluorescence intensity. The effect of self-quenching should also be negligible since it occurs at concentrations about  $10^{-2}$  mol  $L^{-1}$  (López Arbeloa et al. 1989) much larger than the concentrations used in our experiment.

### 3.6 Chemical and velocity fields

During an experiment, we are also interested in keeping track of the interfaces separating the two fluids and in evaluating the amount of mixing that occurs. This is made possible by the different dye concentrations of the two fluids. When the tank is first fully filled with the upper fluid, reference images are made to record the fluorescence intensity in the two spectral bands. During the experiment, the chemical field is then defined as the ratio between images in the “red” spectral band ( $\lambda_2 > 620$  nm) and the uniform upper fluid reference image in the same spectral band at the same  $y$  location. Since the fluorescence intensity does not vary with temperature in the “red” spectral band, this ratio provides us with a good proxy for the fluid composition.

The velocity field is determined by particle image velocimetry (PIV) using the DaVis package from LaVision.

In our Natrosol aqueous solutions, the LDS dye adsorbs on the hydroxyethyl cellulose polymer grains, which provides us with passive tracers. What was initially thought to be a drawback from LDS dye, thus, turned out to be an advantage. Without this effect, the only alternatives would be to remove the filter K21 momentarily to take pictures with the direct laser scattered light or to add glass spheres filled with a fluorescent dye in the fluids, which would both represent additional complications.

## 4 Convection in a two-layer system

Convection in internally heated fluids is governed by two dimensionless numbers, the Prandtl number and the Rayleigh–Roberts number. The Prandtl number represents the ratio of momentum diffusivity over heat diffusivity and is defined by:

$$Pr = \frac{\eta}{\rho\kappa}, \quad (4)$$

where  $\eta$  is dynamic viscosity,  $\rho$  is density, and  $\kappa$  is thermal diffusivity. When  $Pr \gg 1$ , inertial effects are negligible compared to viscous ones. This is the case for Earth’s mantle, where  $Pr > 10^{23}$  as well as in our experiments where  $Pr > 300$ . The Rayleigh–Roberts number that controls the vigor of convection, is:

$$Ra_H = \frac{\rho g \alpha H h^5}{k \kappa \eta}, \quad (5)$$

where  $g$  is the gravitational acceleration,  $\alpha$  is thermal expansivity,  $H$  is the volumetric heat production,  $h$  is the layer thickness and  $k$  is thermal conductivity (Roberts 1967).

The behaviour of a stratified mantle involving two layers with different internal heating rates and densities depends on several dimensionless numbers. Davaille (1999), Le Bars and Davaille (2002) and Davaille et al. (2002) have introduced the buoyancy number,  $B$ :

$$B = \frac{\rho_1 - \rho_2}{\rho_1 \alpha \Delta T}, \quad (6)$$

where  $\rho_1$  and  $\rho_2$  are the lower and upper layers densities respectively, and  $\Delta T$  is the temperature difference driving convection. Depending on the  $B$  value, Le Bars and Davaille (2002) and Davaille et al. (2002) have identified three different regimes in a Rayleigh–Bénard configuration. For  $B > 1$ , the “stratified” regime sees the development of convection in both layers or in only one of them depending on values of the Rayleigh number in each layer while the interface remains flat. Long-lived thermochemical plumes are generated in this regime. In the “whole layer” regime corresponding to  $B < 0.3 - 0.5$ , the interface separating

the two fluid layers is not stable and gets disrupted by convective motions that develop over the whole depth. For intermediate values of  $B$ , the “dynamic topography” regime is such that the interface remains stable in time but is deformed by upwellings and downwellings that develop in the two fluids (Le Bars and Davaille 2004a, b).

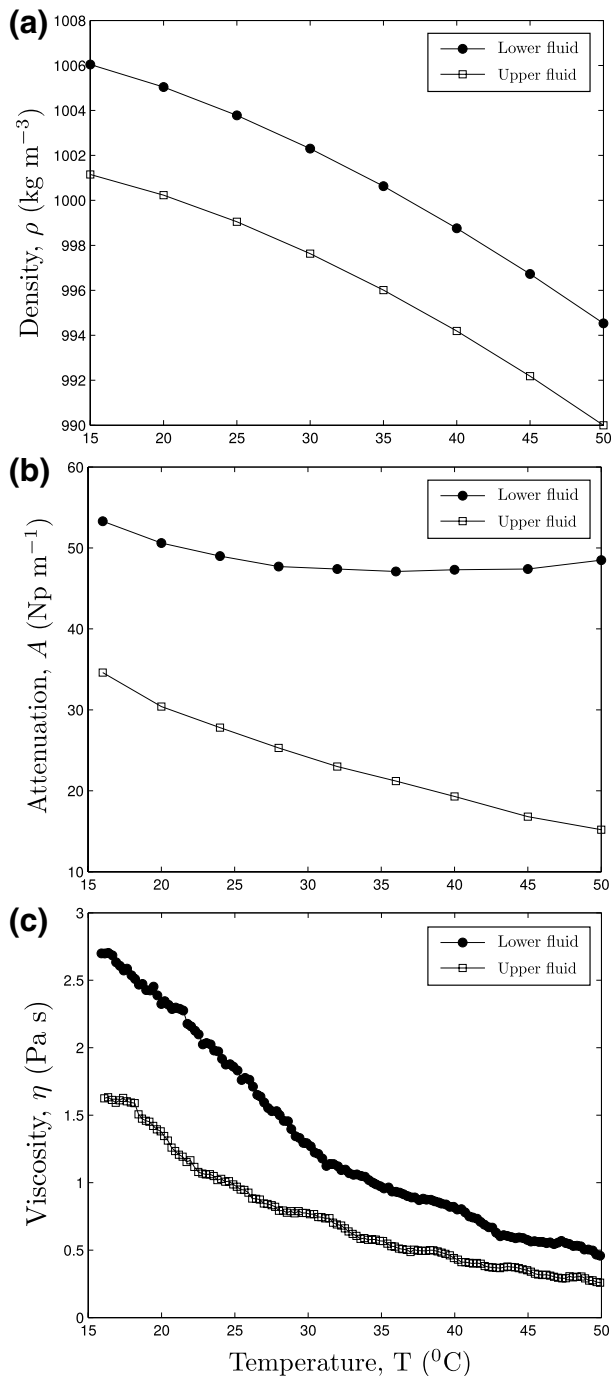


**Fig. 7** Variation of the upper (open squares) and lower (filled black circles) fluid properties with temperature. **a** Density. **b** Attenuation. **c** Viscosity

### 4.1 Fluid properties and dimensionless numbers

We manufactured two different fluids and measured their physical properties in the laboratory. The upper fluid is a 0.6 wt% Natrosol mixture, whereas the lower one is a 0.7 wt% Natrosol mixture with an addition of 0.6 wt% salt. Salt increases both density (Fig. 7a) and microwave absorption (Fig. 7b).

Figure 7c shows that the lower fluid is slightly more viscous than the upper one due to its higher Natrosol concentration. Referring to the lower and upper fluids by indices 1 and 2 respectively, the main control parameters of the experiment are the heat production rate ratio  $H_1/H_2 = 8.8$ , the viscosity ratio  $\eta_1/\eta_2 = 1.9$  and the density contrast  $(\rho_1 - \rho_2)/\rho_1 = 0.48\%$ . The buoyancy number, defined in Eq. 6, is calculated with the maximum temperature difference achieved during the experiment,  $\Delta T_{\text{max}} = 21^{\circ}\text{C}$ , such that  $B = 0.74$ . The Rayleigh–Roberts numbers for the lower and upper fluids are  $Ra_{H_1} = 861.4$  and  $Ra_{H_2} = 2.6 \times 10^4$ , respectively, and the Prandtl numbers are large enough to ensure that inertial effects are negligible. Dye concentrations are three times higher in the lower fluid than in the upper one. Fluid properties and dimensionless numbers are reported in Table 2 for clarity.

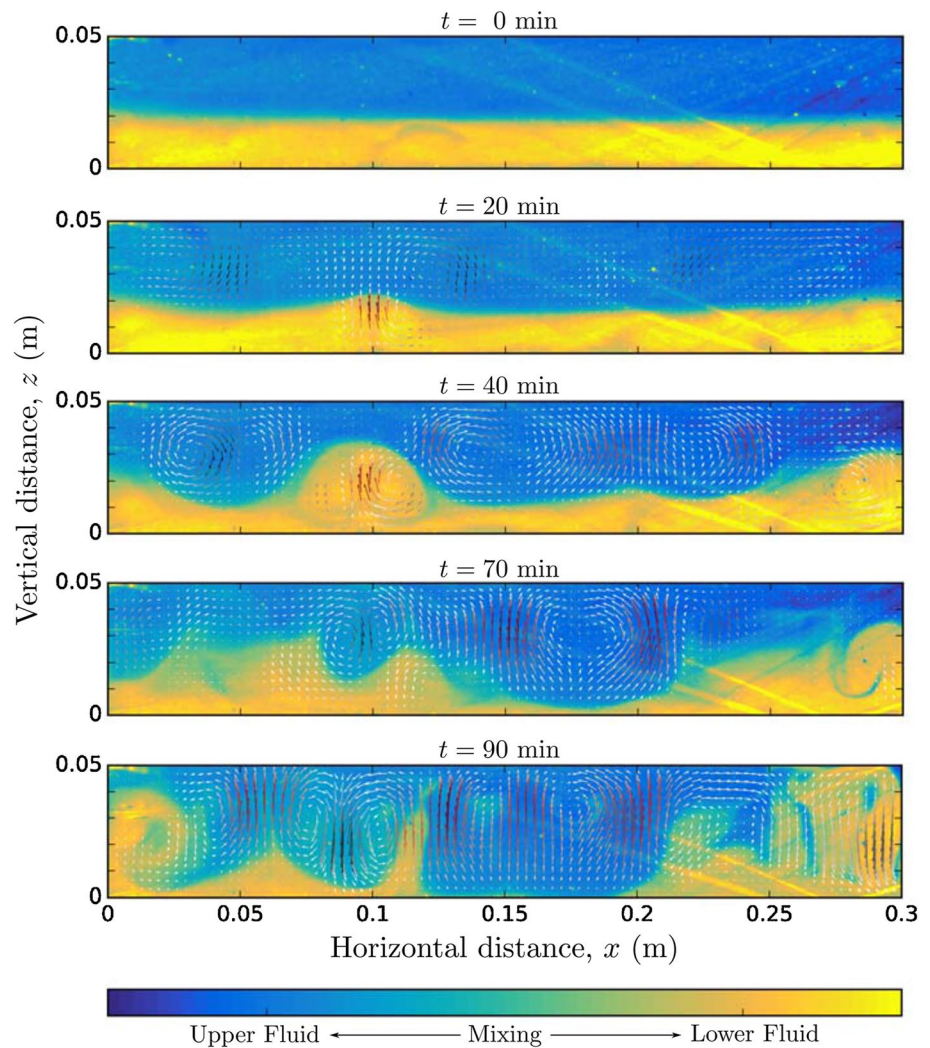
We first filled the tank with the upper fluid and placed it inside the oven to make reference images at room temperature and different y-locations. Then we injected the

**Table 2** Dimensionless numbers and physical properties of the experimental fluids

Physical properties	Lower fluid	Upper fluid
Density ( $\text{kg m}^{-3}$ )	1004.5	999.8
Viscosity (Pa s)	2.16	1.16
Thickness (m)	0.017	0.033
Heat production rate ( $\text{W m}^{-3}$ )	$3.75 \times 10^4$	$4.25 \times 10^3$
Expansivity ( $\text{K}^{-1}$ )	$3.0 \times 10^{-4}$	$2.8 \times 10^{-4}$
Thermal Conductivity ( $\text{W m}^{-1} \text{K}^{-1}$ )	0.6	0.6
Thermal Diffusivity ( $\text{m}^2 \text{s}^{-1}$ )	$1.41 \times 10^{-7}$	$1.41 \times 10^{-7}$
Prandtl number ( $Pr$ )	$1.5 \times 10^4$	$8.2 \times 10^3$
LDS concentration ( $\text{mol L}^{-1}$ )	$10^{-6}$	$3.3 \times 10^{-7}$
FL concentration ( $\text{mol L}^{-1}$ )	$10^{-7}$	$3.3 \times 10^{-8}$
Dimensionless numbers		Experiment
Viscosity ratio ( $\gamma$ )	1.9	
Buoyancy number ( $B$ )	0.74	
Heat production ratio ( $H_1/H_2$ )	8.8	
Thickness ratio ( $h_1/h_2$ )	0.52	
Lower Rayleigh number ( $Ra_{H_1}$ )	861.4	
Upper Rayleigh number ( $Ra_{H_2}$ )	$2.6 \times 10^4$	

Values are given at a temperature of 22  $^{\circ}\text{C}$

**Fig. 8** Time evolution of the chemical and velocity fields at  $y = 0.04$  m. Colorscale for composition goes from *blue* (upper fluid) to *light orange* (lower fluid), with *green shading* indicative of mixing between the two fluids. The velocity magnitude increases with time but this is not reflected in the lengths of arrows for clarity. The velocity colorscale is tied to the vertical velocity component, *arrows* are *white* for horizontal flow and go from *black* for downwellings to *dark red* for upwellings



denser lower fluid and let it spread at the base of the tank. The thickness of the lower layer was  $1.7$  cm leading to  $h_1/h_2 = 0.52$ . Power was turned on at  $70$  W and kept for  $90$  min.

## 4.2 Convection dynamics

Figure 8 shows the evolution of composition with time as well as the velocity field in a vertical cross section at a distance of  $0.04$  m from the side-wall. Convection develops first in the upper layer, as may be expected from the large value of the Rayleigh–Roberts number, at about  $1.3$  min. The lower layer starts to deform at  $t = 20$  min, with two large domes that grow at  $x = 0.10$  m and  $x = 0.28$  m. At the same time, three downwellings are visible in the upper layer in  $x = 0.05$ ,  $0.14$  and  $0.23$  m. At  $t = 40$  min, the lower layer domes continue to grow and the distribution of dye concentration reveals an internal fluid circulation showing up as two vortices in this vertical cross section. Green wisps in the upper fluid show that parts

of the lower fluid get sheared out off the domes and mix with the upper fluid. This phenomenon is most active at the lateral edges of the domes. On this 2-D section (at  $y = 0.04$  m), the large-scale flow structure is illustrated very well by the velocity field, which is oriented upwards or downwards over large horizontal distances. The lower layer has been disrupted very significantly at  $t = 70$  min and has been almost completely thinned out in some areas at  $t = 90$  min. One observes a number of irregular regions of lower fluid that protrude into the upper one and change shape as they grow taller. Some of them eventually fold and fall back on themselves, encapsulating upper fluid as they collapse. This is an efficient mixing mechanism able to process significant volumes of upper fluid but it is only active intermittently. In comparison, shearing of lower fluid at the edge of the protrusions occurs continuously.

Globally, the lower fluid exhibits a form of up and down motion that is reminiscent of the oscillatory regime of two-layer Rayleigh–Bénard convection. One large difference,

however, is that, due to their higher heat generation rate, the protrusions of lower fluid are more stable because they are able to remain hotter than the surrounding fluid for longer. Such stability is also responsible for their dramatic changes of shape. Tall protrusions supply heat to the encasing upper fluid, thereby driving edge upwellings that stretch them further. At the end of the sequence, one is left with a number of “piles” with a range of shapes at the base of the tank. Some thin regions of lower fluid have been stretched in the vertical direction and have reached the top of the tank despite their large intrinsic density.

Due to the large light intensity contrast between the two fluids, we were able to track the interface that separates them and to reconstruct the lower layer morphology in 3D. For computational reasons, we decreased the spatial resolution down to one pixel per millimeter in the zone of interest. Figure 9 shows the morphology of the lower layer at three different times together with the mean vertical velocities above and below its highly contorted upper boundary. The interface deformation is due to motions in both the upper and lower fluids and it may be somewhat artificial to distinguish between the two contributions. It is important, however, to elucidate the main control on the scale of deformation. At  $t = 35$  min (Fig. 9a), several domes grow from the lower layer whilst upper fluid from the large downwellings that developed first spreads out, displacing lower fluid laterally, as shown at  $t = 55$  min in Fig. 9b. The domes are arranged in two quasi parallel ridges made of several

individuals, whereas these ridges are separated by a distance that is much larger than that of the domes. This pattern can be understood as the superposition of two patterns at different scales: the large-scale pattern is determined by the upper layer (the distance between the two ridges), while the smaller scale pattern is instead determined by the lower layer (the distance between neighbouring domes). As the domes grow taller, they heat up the surrounding upper fluid at their edges, generating local upwellings that drive a cellular pattern at a smaller scale than that of the large initial downwellings.

This experiment can be classified as being in the regime called “hybrid” by Davaille (1999) because it is characterized by oscillatory doming and a long-lived layer of lower fluid at the base of the tank. This is consistent with the “intermediate” value of the buoyancy number ( $B = 0.74$ ).

### 4.3 Mixing and changes of thermal structure

We are able to track the interface that separates the two fluids and hence to determine the volume of the lower layer as time progresses. When mixing occurs, and parts of the lower fluid get entrained into the upper one, the fluorescence intensity decreases (from yellow to green in Fig. 8) and becomes lower than the threshold value that separates the two fluids. Knowing the volume of one pixel ( $1 \text{ mm}^3$ ), we simply count the number of pixels

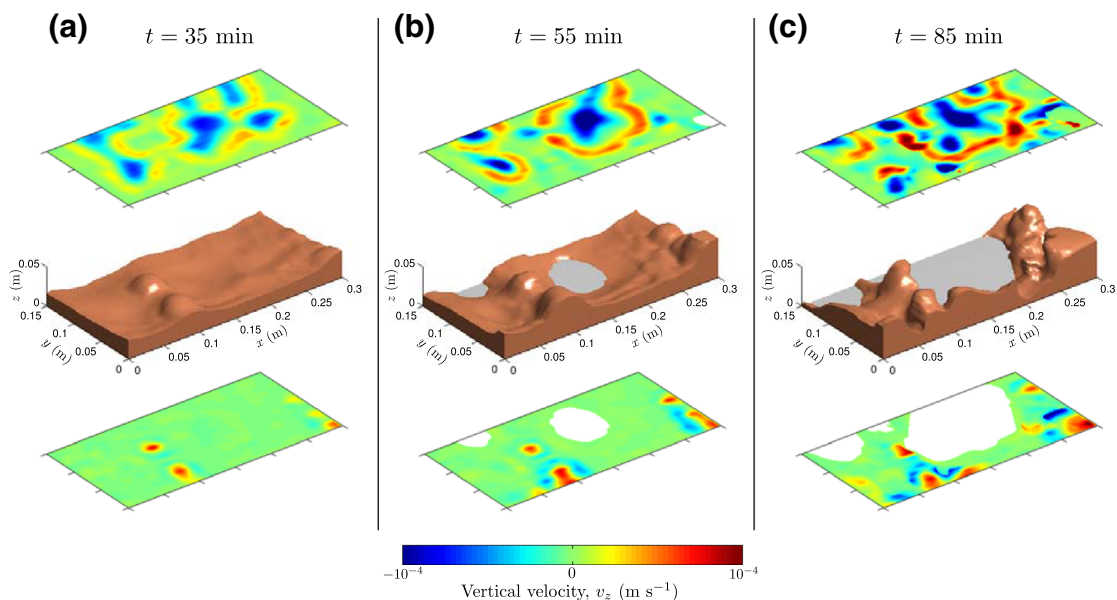


**Fig. 9** Reconstructed lower layer topography (*brown structures in middle panels*) and maps of the averaged vertical velocity above (*top panels*) and below (*bottom panels*) the interface between the two fluids. Data are shown at three different times: **a**  $t = 35$  min, **b**  $t = 55$

min, **c**  $t = 85$  min. In *middle panels*, *grey shaded areas* are the very base of the tank. The main upwellings in the upper layer are concentrated at the edges of uplifted regions in the lower layer

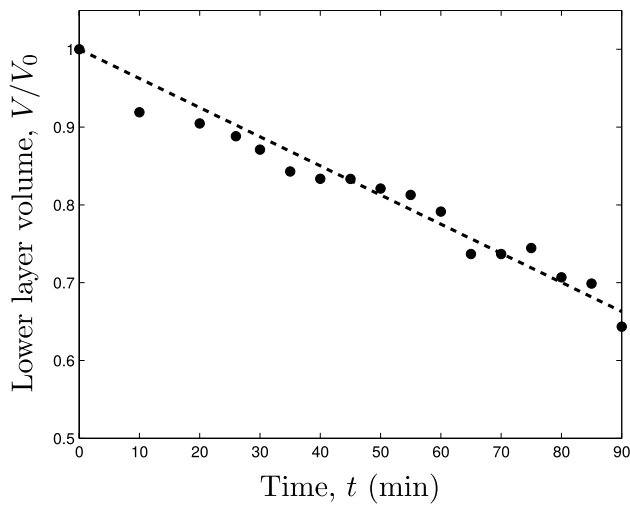


**Fig. 10** Evolution in time of the lower layer volume scaled by its initial value  $V_0$ . Dashed line is the best linear fit corresponding to Eq. 7 with  $C_1 = 0.23$

with a light intensity greater than the threshold value. With only a threshold intensity value, it is not possible to locate the interface with precision everywhere but we estimate that the maximum systematic error is one pixel (i.e., 1 mm). The evolution of the lower layer volume is shown in Fig. 10. The lower fluid is progressively eroded by convective currents in the upper layer leading to a 35% decrease of its initial volume over the course of the experiment. A straight line allows a reasonable fit to the data, indicating a roughly constant rate of mixing equal to  $\approx 0.1 \text{ cm}^3 \text{ s}^{-1}$ . Departures from the straight line are not random, however, and can be correlated with the amplitude of the interface deformation. The largest rates of mixing are achieved when interface deformation is maximum.

Davaille et al. (2002) showed that, in the case of thin lower layers ( $h_1/h_2 < 0.2$ ), the rate of mixing across the interface,  $Q_m$ , can be deduced from a balance between buoyancy and viscous forces, such that:

$$Q_m = C_1 \kappa L B_l^{-2} Ra_p^{1/3} \frac{1}{1 + \gamma/B_l},$$

where  $B_l = \frac{\Delta\rho}{\rho\alpha\theta}$ ,

and  $Ra_p = \frac{\alpha g \theta L^3}{\kappa \nu}$ ,

where  $C_1$  is an experimental constant,  $\theta$  is the temperature anomaly associated with thermochemical plumes and  $L$  is the lateral distance between them. In our case, entrainment occurs mainly at the edges of protrusions and piles, where upwellings of upper fluid shear thin wisps of lower fluid out. The distance  $L$  is therefore the spacing

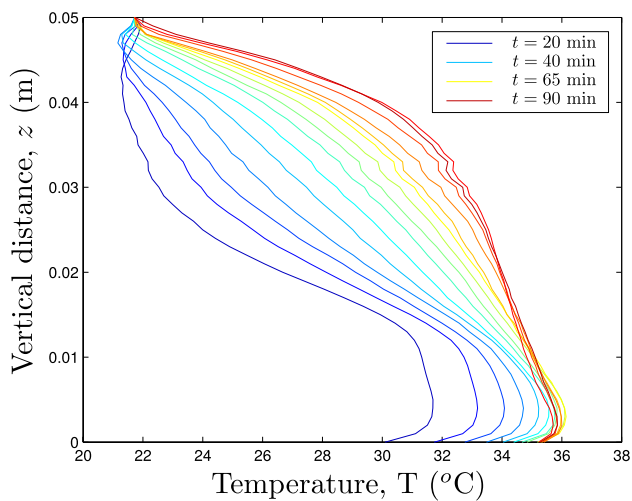
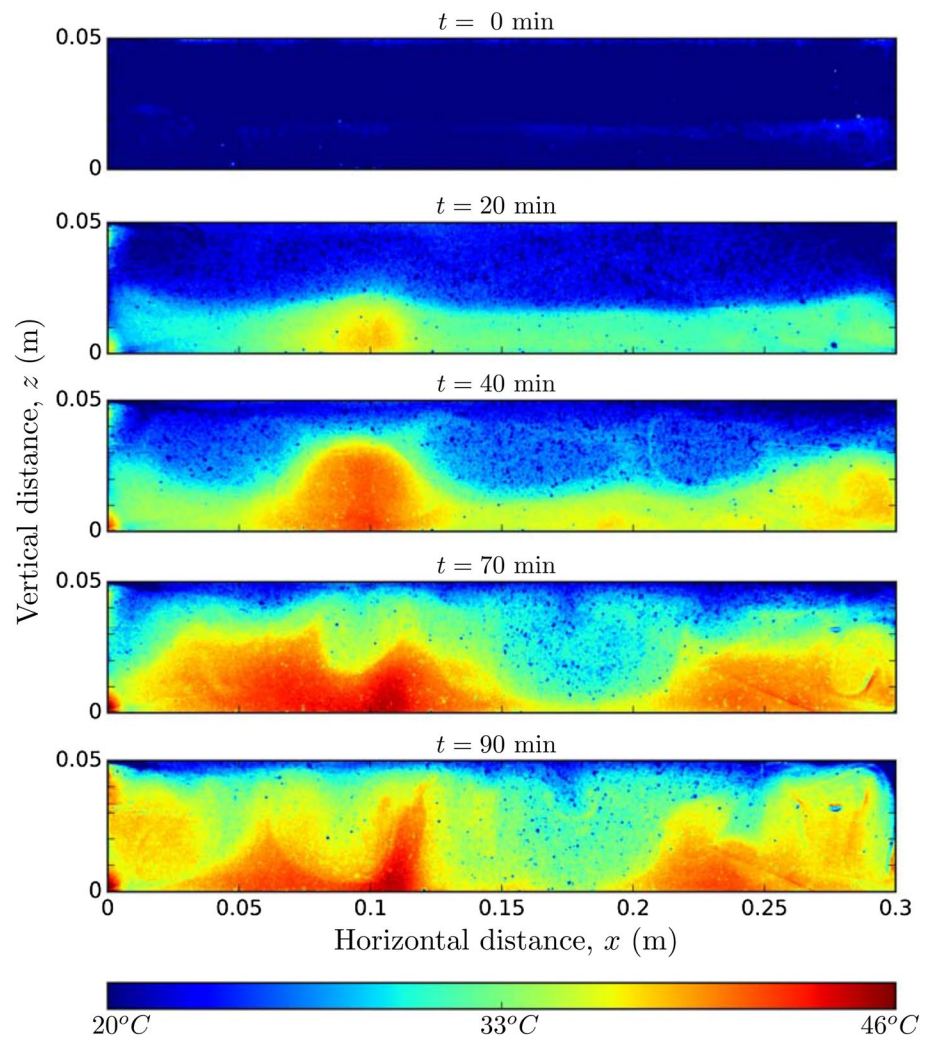
separating downwellings in the upper layer. When convection is fully developed, we can count between 5 and 6 such downwellings (see Fig. 9b, c), implying that  $L \approx 0.10 \text{ m}$ . From the observed temperature anomaly inside a protrusion (Fig. 11), we take  $\theta = 19^\circ\text{C}$ . Inserting these values together with the parameters in Table 2 in Eq. 7, we deduce that  $C_1 = 0.23$  from the data of Fig. 10. This value compares well with the results of Gonnermann et al. (2002) ( $C_1 = 0.2$ ) and Davaille et al. (2002) ( $C_1 = 0.61$ ), two independent experimental studies that investigated entrainment in a two-layered convective system heated from below.

Figure 11 shows how the temperature field evolves with time in a vertical cross section located at  $y = 0.04 \text{ m}$ . The impact of a larger internal heat production in the lower fluid is clearly visible. At  $t = 20 \text{ min}$ , the lower layer is on the whole warmer than the upper layer and the interior of protrusions is  $14^\circ\text{C}$  hotter than the surrounding lower fluid. The temperature profile at  $t = 40 \text{ min}$  records the effect of the smaller plumes that are visible at  $x = 0.12, 0.2$  and  $0.25 \text{ m}$ . As the convection vigor increases, such small-scale features are less prominent. When convection in the upper layer dominates the flow structure, i.e., at  $t = 70 \text{ min}$ , the upper thermal boundary layer becomes visible in dark blue in the temperature signal. At  $t = 90 \text{ min}$ , the warmest parts of the tank are in the piles at the base.

With our scanning procedure, we are able to average temperatures in both horizontal directions. Figure 12 shows the resulting vertical profiles during our experiment. Uncertainties in temperature values are largest at the top and bottom of the tank due to laser reflections on the horizontal bounding plates. The system clearly evolves from a well-separated two-layered system with a lower layer  $9^\circ\text{C}$  hotter than the upper one, to an apparently single layer where temperature increases with depth in monotonous fashion. Temperature profiles at later times are characterized by a single well-developed thermal boundary layer at the top overlying an interior region with an almost constant temperature gradient. The vertical temperature gradient is very small at the base of the tank, as appropriate for an adiabatic lower boundary (the situation at early times is discussed below). An important result is that, below the boundary layer at the top, the fluid interior is not at a uniform temperature, in marked contrast with the structure of a homogeneous internally heated fluid. The lack of a marked transition in the interior temperature profile is due to the stretching of lower fluid parcels into the upper fluid, such that the fraction of lower fluid in a horizontal cross section decreases gradually with increasing height above the base.

At early times, the vertical temperature gradient at the base of the tank is not zero (Fig. 12), due to the thermal inertia of the lower plate, which lags behind the interior fluid. This leads to a very thin layer that is stably stratified thermally and whose thickness is decreasing with time.

**Fig. 11** Time evolution of the temperature distribution at  $y = 0.04$  m. The grainy texture of the images is due to LDS adsorption on Natrosol grains. Small-scale convection occurs at the interface at  $t = 40$  min. The largest temperatures are reached in the piles of lower fluid at the base of the tank



**Fig. 12** Averaged vertical temperature profiles at different times during the experiment. Colours indicate time evolution from dark blue to dark red. The two-layered system is well defined in temperature at  $t = 20$  min with a bottom layer warmer than the top layer. It clearly evolves towards a one-layer vertical temperature profile as piles form and the two fluids are being mixed by convective process

This layer cannot generate convective motions and is not expected to affect the dynamics significantly.

## 5 Discussion: coherent structures at the base of the convecting layer

We have shown results for only one experiment, but it is worth discussing the structures that develop out of the basal layer. Figure 13 summarizes the different coherent structures that have been observed at different locations and at different times. Protrusions of lower fluid into the upper fluid take various forms, including rounded domes (Fig. 13a), broad plumes (Fig. 13b), or flat domes (Fig. 13c). Rounded domes are a well-known feature of oscillatory convection (Le Bars and Davaille 2004b) and can take “mexican hat” shapes as they collapse on themselves (Fig. 13d). Morphologies evolve into ridge-like linear structures (Fig. 13e) and pointed cones (Fig. 13f). Excepting large rounded domes that can only deform over very long time intervals, most structures are modified

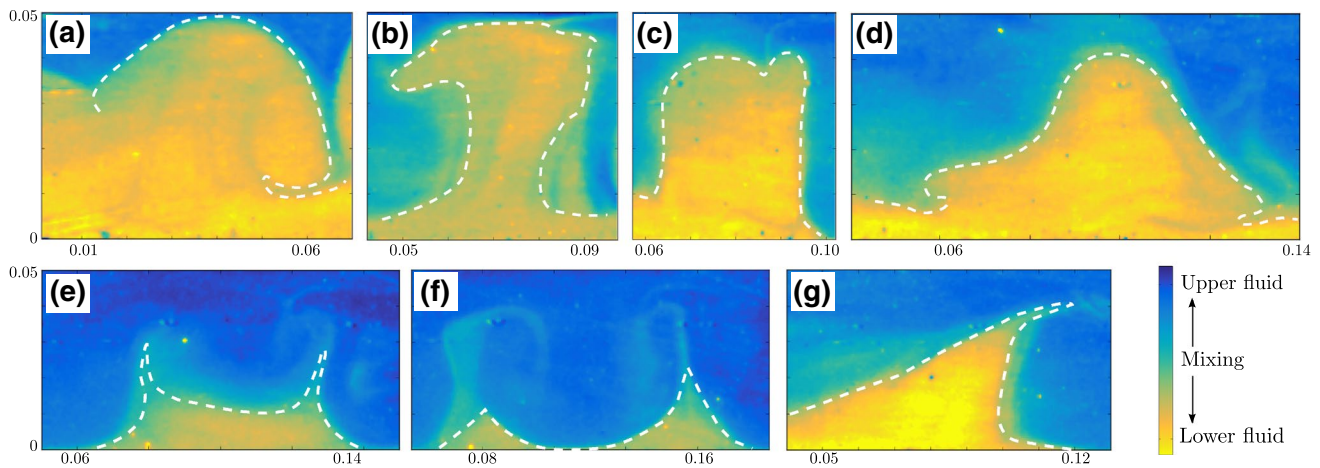


**Fig. 13** Catalogue of morphologies taken by the lower layer. **a** Rounded dome ( $y = 0$  m,  $t = 70$  min). **b** Broad plume ( $y = 0.01$  m,  $t = 90$  min). **c** Flat dome ( $y = 0.05$  m,  $t = 80$  min). **d** “mexican hat”

dome ( $y = 0.04$  m,  $t = 60$  min). **e** Ridge-like pile ( $y = 0.13$  m,  $t = 80$  min). **f** Pointed cones ( $y = 0.14$  m,  $t = 85$  min). **g** Overhanging cone ( $y = 0.08$  m,  $t = 80$  min)

relatively rapidly by the vigorous motions of the upper fluid. These structures do not move around rapidly, however, and remain at approximately the same locations as they get stretched and folded, as illustrated clearly by Fig. 9. For application to the Earth’s mantle, the relevant time spans must be properly scaled, which is outside the scope of the present paper. We note, however, that these structures survive through a large number of upper boundary layer instabilities and throughout the whole transient heating phase that leads to convection in a steady-state.

The relevance of the present work can be assessed by comparing our findings to those of earlier two-layer convection studies and to the LLSVP structures that have been detected at the core–mantle boundary. Flat domes, ridge-like elongated piles and pointed cones have all been observed in numerical simulations (Tackley 2002; McNamara and Zhong 2005; Tan and Gurnis 2005; Li et al. 2014) and laboratory experiments (Jellinek and Manga 2002; Gonnermann et al. 2002) involving systems with a strong degree of compositional stratification. The asymmetrical deformed conical structure shown in Fig. 13g with an overhanging boundary on one side is very close to the LLSVP that lies below the East African Rift (Cot-taar and Lekic 2016). In our experiments, the strongest and most focussed upwellings are generated at the edges of tall piles, which could explain why hot-spot volcanoes seem to originate from the periphery of the broad LLSVPs detected by seismic tomography (French and Romanowicz 2015).

## 6 Conclusion

We have designed a new experimental protocol to study convection driven by internal heat sources in heterogeneous fluid layers. Ratiometric laser-induced fluorescence is

used to determine temperature in the fluid interior within a 5% accuracy. Local values of composition and velocity are also determined. This protocol was tested successfully in an experiment aimed at understanding the stability and longevity of a compositionally dense layer that is enriched in radioactive elements at the base of a larger system, which is relevant to the Earth’s mantle. We have shown that, in a such convecting system, the lower fluid, which is hotter but compositionally denser than the upper one, interacts dynamically with the overlying fluid. In particular, the interface between the two fluids gets deformed by large amounts due to both hot upwellings in the lower layer and cold downwellings in the upper layer. This interaction eventually leads to the formation of relatively stable piles with a great variety of shapes, which are reminiscent of structures that have been imaged by seismic tomography above the core–mantle boundary. Mixing between the two fluids leads to a steadily decreasing amount of lower fluid in the system and to an upper material that is a mixture of the two original fluids. A key result is the relationship between the intensity of mixing and the amplitude of deformation in the lower layer. One factor is obviously the enhanced contact area that is achieved by the deformation but an equally important one is the vigour of the local upwellings that are generated at the edges of tall piles. One consequence of mixing, of course, is that the amount of distinctive lower mantle material that now exists in the Earth may be a small fraction of the initial one. In these conditions, the current convection regime and deep structure of the Earth’s mantle and the location and number of hotspots must be understood as resulting from four billions of years of evolution of a heterogeneous reservoir. Our experimental method is particularly well-suited to the analysis of such a system.

**Acknowledgements** This work was funded by the PNP-INSU 2016 Grant as well as the ANR-11-IS04-0004 project for the French team and by the 1 RO-FR-22-2011 Romanian–French bilateral project for the Romanian team. We thank the laboratory of Géochimie des Eaux in IPGP and especially Pr. Marc Benedetti for guiding us with insightful information on how to use their spectrofluorometers in order to analyze the fluorescent properties of the dyes and filters used in this study. IPGP contribution No 3855.

## References

- Andrews D (1989) A unified theory of radiative and radiationless molecular energy transfer. *Chem Phys* 135(2):195–201. doi:[10.1016/0301-0104\(89\)87019-3](https://doi.org/10.1016/0301-0104(89)87019-3)
- Arevalo R, McDonough WF, Stracke A, Willbold M, Ireland TJ, Walker RJ (2013) Simplified mantle architecture and distribution of radiogenic power. *Geochem Geophys Geosyst* 14:2265–2285. doi:[10.1002/ggge.20152](https://doi.org/10.1002/ggge.20152)
- Boyet M, Carlson RW (2005)  $^{142}\text{Nd}$  evidence for early (>4.53 ga) global differentiation of the silicate earth. *Science* 309:576–581. doi:[10.1126/science.1113634](https://doi.org/10.1126/science.1113634)
- Bruchhausen M, Guillard F, Lemoine F (2005) Instantaneous measurement of two-dimensional temperature distributions by means of two-color planar laser induced fluorescence (PLIF). *Exp Fluids* 38:123–131. doi:[10.1007/s00348-004-0911-2](https://doi.org/10.1007/s00348-004-0911-2)
- Coppeta J, Rogers C (1998) Dual emission laser induced fluorescence for direct planar scalar behavior measurements. *Exp Fluids* 25:1–15
- Cottaar S, Lekic V (2016) Morphology of seismically slow lower-mantle structures. *Geophys J Int* 207:1122–1136. doi:[10.1093/gji/ggw324](https://doi.org/10.1093/gji/ggw324)
- Dadarlat D, Neamtu C (2009) High performance photopyroelectric calorimetry of liquids. *Acta Chim Slov* 56:225–236
- Davaille A (1999) Simultaneous generation of hotspots and superswells by convection in a heterogeneous planetary mantle. *Nature* 402:756–760. doi:[10.1038/45461](https://doi.org/10.1038/45461)
- Davaille A, Limare A (2015) 7.03 - Laboratory Studies of Mantle Convection. In: Schubert G (ed) *Treatise on Geophysics*, 2nd edn, Elsevier, Oxford, pp 73–144. doi:[10.1016/B978-0-444-53802-4.00128-7](https://doi.org/10.1016/B978-0-444-53802-4.00128-7)
- Davaille A, Girard F, Le Bars M (2002) How to anchor hotspots in a convecting mantle? *Earth Planet Sci Lett* 203:621–634. doi:[10.1016/S0012-821X\(02\)00897-X](https://doi.org/10.1016/S0012-821X(02)00897-X)
- Davies DR, Davies JH, Hassan O, Morgan K, Nithiarasu P (2007) Investigations into the applicability of adaptive finite element methods to two-dimensional infinite Prandtl number thermal and thermochemical convection. *Geochem Geophys Geosyst* 8:Q05010. doi:[10.1029/2006GC001470](https://doi.org/10.1029/2006GC001470)
- Davies DR, Goes S, Lau HCP (2015) *Thermally dominated deep mantle LLSVPs: a review*. Springer, Cham, pp 441–477. doi:[10.1007/978-3-319-15627-9\\_14](https://doi.org/10.1007/978-3-319-15627-9_14)
- Deschamps F, Tackley PJ (2008) Searching for models of thermochemical convection that explain probabilistic tomography. I. Principles and influence of rheological parameters. *Phys Earth Planet Int* 171:357–373. doi:[10.1016/j.pepi.2008.04.016](https://doi.org/10.1016/j.pepi.2008.04.016)
- Deschamps F, Tackley PJ (2009) Searching for models of thermochemical convection that explain probabilistic tomography. II- Influence of physical and compositional parameters. *Phys Earth Planet Int* 176:1–18. doi:[10.1016/j.pepi.2009.03.012](https://doi.org/10.1016/j.pepi.2009.03.012)
- Dziewonski AM (1984) Mapping the Lower Mantle: determination of lateral heterogeneity in P velocity up to degree and order 6. *J Geophys Res* 89:5929–5952. doi:[10.1029/JB089iB07p05929](https://doi.org/10.1029/JB089iB07p05929)
- French SW, Romanowicz B (2015) Broad plumes rooted at the base of the Earth's mantle beneath major hotspots. *Nature* 525:95–99. doi:[10.1038/nature14876](https://doi.org/10.1038/nature14876)
- Funatani S, Fujisawa N, Ikeda H (2004) Simultaneous measurement of temperature and velocity using two-colour LIF combined with PIV with a colour CCD camera and its application to the turbulent buoyant plume. *Meas Sci Technol* 15:983–990. doi:[10.1088/0957-0233/15/5/030](https://doi.org/10.1088/0957-0233/15/5/030)
- Garnero EJ, McNamara AK, Shim SH (2016) Continent-sized anomalous zones with low seismic velocity at the base of Earth's mantle. *Nat Geosci* 9:481–489. doi:[10.1038/ngeo2733](https://doi.org/10.1038/ngeo2733)
- Geddes CD (2001) Optical halide sensing using fluorescence quenching: theory, simulations and applications - a review. *Meas Sci Technol* 12(9):R53
- Gonnermann HM, Manga M, Mark Jellinek A (2002) Dynamics and longevity of an initially stratified mantle. *Geophys Res Lett* 29:1399. doi:[10.1029/2002GL014851](https://doi.org/10.1029/2002GL014851)
- Hishida K, Sakakibara J (2000) Combined planar laser-induced fluorescence-particle image velocimetry technique for velocity and temperature fields. *Exp Fluids* 29:129–140
- Hofmann AW (1997) Mantle geochemistry: the message from oceanic volcanism. *Nature* 385:219–229. doi:[10.1038/385219a0](https://doi.org/10.1038/385219a0)
- Jaupart C, Labrosse S, Lucazeau F, Mareschal JC (2015) 7.06 - Temperatures, Heat, and Energy in the Mantle of the Earth. In: Schubert G (ed) *Treatise on geophysics* (2nd edn), Elsevier, Oxford, pp 223–270. doi:[10.1016/B978-0-444-53802-4.00126-3](https://doi.org/10.1016/B978-0-444-53802-4.00126-3)
- Javoy M, Kaminski E (2014) Earth's Uranium and Thorium content and geoneutrinos fluxes based on enstatite chondrites. *Earth Planet Sci Lett* 407:1–8. doi:[10.1016/j.epsl.2014.09.028](https://doi.org/10.1016/j.epsl.2014.09.028)
- Jellinek AM, Manga M (2002) The influence of a chemical boundary layer on the fixity, spacing and lifetime of mantle plumes. *Nature* 418:760–763
- Kaminski E, Javoy M (2013) A two-stage scenario for the formation of the Earth's mantle and core. *Earth Planet Sci Lett* 365:97–107. doi:[10.1016/j.epsl.2013.01.025](https://doi.org/10.1016/j.epsl.2013.01.025)
- Kellogg LH, Hager BH, van der Hilst RD (1999) Compositional stratification in the deep mantle. *Science* 283:1881. doi:[10.1126/science.283.5409.1881](https://doi.org/10.1126/science.283.5409.1881)
- Kulacki FA, Goldstein RJ (1972) Thermal convection in a horizontal fluid layer with uniform volumetric energy sources. *J Fluid Mech* 55:271–287. doi:[10.1017/S0022112072001855](https://doi.org/10.1017/S0022112072001855)
- Kulacki FA, Nagle ME (1975) Natural convection in a horizontal fluid layer with volumetric energy sources. *J Heat Transf* 97:204–211. doi:[10.1115/1.3450342](https://doi.org/10.1115/1.3450342)
- Labrosse S, Hernlund JW, Coltice N (2007) A crystallizing dense magma ocean at the base of the Earth's mantle. *Nature* 450:866–869. doi:[10.1038/nature06355](https://doi.org/10.1038/nature06355)
- Le Bars M, Davaille A (2002) Stability of thermal convection in two superimposed miscible viscous fluids. *J Fluid Mech* 471:339–363. doi:[10.1017/S0022112002001878](https://doi.org/10.1017/S0022112002001878)
- Le Bars M, Davaille A (2004a) Large interface deformation in two-layer thermal convection of miscible viscous fluids. *J Fluid Mech* 499:75–110. doi:[10.1017/S0022112003006931](https://doi.org/10.1017/S0022112003006931)
- Le Bars M, Davaille A (2004b) Whole layer convection in a heterogeneous planetary mantle. *J Geophys Res Solid Earth* 109:B03403. doi:[10.1029/2003JB002617](https://doi.org/10.1029/2003JB002617)
- Lekic V, Cottaar S, Dziewonski A, Romanowicz B (2012) Cluster analysis of global lower mantle tomography: a new class of structure and implications for chemical heterogeneity. *Earth Planet Sci Lett* 357:68–77. doi:[10.1016/j.epsl.2012.09.014](https://doi.org/10.1016/j.epsl.2012.09.014)
- Lemoine F, Antoine Y, Wolff M, Leboche M (1999) Simultaneous temperature and 2D velocity measurements in a turbulent heated jet using combined laser-induced fluorescence and LDA. *Exp Fluids* 26:315–323
- Leng W, Zhong S (2011) Implementation and application of adaptive mesh refinement for thermochemical mantle convection studies. *Geochem Geophys Geosyst* 12:Q04006. doi:[10.1029/2010GC003425](https://doi.org/10.1029/2010GC003425)

- Li M, McNamara AK, Garnero EJ (2014) Chemical complexity of hotspots caused by cycling oceanic crust through mantle reservoirs. *Nat Geosci* 7:366–370. doi:[10.1038/ngeo2120](https://doi.org/10.1038/ngeo2120)
- Limare A, Surducan E, Surducan V, Neamtu C, di Giuseppe E, Vilella K, Farnetani CG, Kaminski E, Jaupart C (2013) Microwave-based laboratory experiments for internally-heated mantle convection. In: Lazar MD, Garabagiu S (eds) American Institute of Physics Conference Series, American Institute of Physics Conference Series, vol 1565, pp 14–18. doi:[10.1063/1.4833687](https://doi.org/10.1063/1.4833687)
- Limare A, Vilella K, Di Giuseppe E, Farnetani CG, Kaminski E, Surducan E, Surducan V, Neamtu C, Fourel L, Jaupart C (2015) Microwave-heating laboratory experiments for planetary mantle convection. *J Fluid Mech* 777:50–67. doi:[10.1017/jfm.2015.347](https://doi.org/10.1017/jfm.2015.347)
- López Arbeloa F, Ruiz Ojeda P, López Arbeloa I (1989) Fluorescence self-quenching of the molecular forms of rhodamine b in aqueous and ethanolic solutions. *J Lumin* 44:105–112. doi:[10.1016/0022-2313\(89\)90027-6](https://doi.org/10.1016/0022-2313(89)90027-6)
- Masters G, Laske G, Bolton H, Dziewonski A (2000) The relative behavior of shear velocity, bulk sound speed, and compressional velocity in the mantle: Implications for chemical and thermal structure. *Wash DC Am Geophys Union Geophys Monogr Ser* 117:63–87. doi:[10.1029/GM117p0063](https://doi.org/10.1029/GM117p0063)
- McDonough W, Sun S (1995) The composition of the earth. *Chem Geol* 120(3):223–253. doi:[10.1016/0009-2541\(94\)00140-4](https://doi.org/10.1016/0009-2541(94)00140-4)
- McNamara AK, Zhong S (2005) Thermochemical structures beneath Africa and the Pacific Ocean. *Nature* 437:1136–1139. doi:[10.1038/nature04066](https://doi.org/10.1038/nature04066)
- Moreira M, Breddam K, Curtice J, Kurz MD (2001) Solar neon in the Icelandic mantle: new evidence for an undegassed lower mantle. *Earth Planet Sci Lett* 185:15–23. doi:[10.1016/S0012-821X\(00\)00351-4](https://doi.org/10.1016/S0012-821X(00)00351-4)
- Nakagawa T, Tackley PJ (2014) Influence of combined primordial layering and recycled MORB on the coupled thermal evolution of Earth's mantle and core. *Geochem Geophys Geosyst* 15:619–633. doi:[10.1002/2013GC005128](https://doi.org/10.1002/2013GC005128)
- Roberts PH (1967) Convection in horizontal layers with internal heat generation. *Theory. J Fluid Mech* 30:33–49. doi:[10.1017/S0022112067001284](https://doi.org/10.1017/S0022112067001284)
- Sakakibara J, Adrian RJ (1999) Whole field measurement of temperature in water using two-color laser induced fluorescence. *Exp Fluids* 26:7–15
- Sakakibara J, Adrian RJ (2004) Measurement of temperature field of a Rayleigh–Bénard convection using two-color laser-induced fluorescence. *Exp Fluids* 37:331–340. doi:[10.1007/s00348-004-0821-3](https://doi.org/10.1007/s00348-004-0821-3)
- Schwiderski EW, Schwab HJA (1971) Convection experiments with electrolytically heated fluid layers. *J Fluid Mech* 48:703–719. doi:[10.1017/S0022112071001812](https://doi.org/10.1017/S0022112071001812)
- Surducan E, Surducan V (2014) Device for connecting a camera to a treatment enclosure under power microwave field for taking real time images of a processed sample (in romanian). In: *Buletinul Oficial de Proprietate Industrială, Bucharest, Romania*, p 48. [http://www.osim.ro/publicatii/brevete/bopi\\_2014/bopi\\_inv\\_02\\_2014.pdf](http://www.osim.ro/publicatii/brevete/bopi_2014/bopi_inv_02_2014.pdf), patent pending RO129276 (A2)
- Surducan E, Surducan V, Neamtu C (2012) Measurements of the liquids dielectric properties changes with temperature for microwaves power processing optimization. In: Lazar MD (ed) American institute of physics conference series, vol 1425, pp 85–88. doi:[10.1063/1.3681973](https://doi.org/10.1063/1.3681973)
- Surducan E, Surducan V, Limare A, Neamtu C, Di Giuseppe E (2014) Microwave heating device for internal heating convection experiments, applied to Earth's mantle dynamics. *Rev Sci Instrum* 85(12):124702. doi:[10.1063/1.4902323](https://doi.org/10.1063/1.4902323)
- Sutton JA, Fisher BT, Fleming JW (2008) A laser-induced fluorescence measurement for aqueous fluid flows with improved temperature sensitivity. *Exp Fluids* 45:869–881. doi:[10.1007/s00348-008-0506-4](https://doi.org/10.1007/s00348-008-0506-4)
- Tackley PJ (2002) Strong heterogeneity caused by deep mantle layering. *Geochem Geophys Geosyst* 3:1024. doi:[10.1029/2001GC000167](https://doi.org/10.1029/2001GC000167)
- Takahashi J, Tasaka Y, Murai Y, Takeda Y, Yanagisawa T (2010) Experimental study of cell pattern formation induced by internal heat sources in a horizontal fluid layer. *Int J Heat Mass Transf* 53(7–8):1483–1490. doi:[10.1016/j.ijheatmasstransfer.2009.11.048](https://doi.org/10.1016/j.ijheatmasstransfer.2009.11.048)
- Tan E, Gurnis M (2005) Metastable superplumes and mantle compressibility. *Geophys Res Lett* 32:L20307. doi:[10.1029/2005GL024190](https://doi.org/10.1029/2005GL024190)
- Tasaka Y, Kudoh Y, Takeda Y, Yanagisawa T (2005) Experimental investigation of natural convection induced by internal heat generation. In: Takeda Y (ed) *Journal of physics conference series*, vol 14, pp 168–179. doi:[10.1088/1742-6596/14/1/021](https://doi.org/10.1088/1742-6596/14/1/021)
- Torsvik TH, Steinberger B, Cocks LRM, Burke K (2008) Longitude: linking earth's ancient surface to its deep interior. *Earth Planet Sci Lett* 276:273–282. doi:[10.1016/j.epsl.2008.09.026](https://doi.org/10.1016/j.epsl.2008.09.026)
- Tritton DJ, Zarraga MN (1967) Convection in horizontal layers with internal heat generation. *Experiments. J Fluid Mech* 30:21–31. doi:[10.1017/S0022112067001272](https://doi.org/10.1017/S0022112067001272)
- van Keken PE, King SD, Schmeling H, Christensen UR, Neumeister D, Doin MP (1997) A comparison of methods for the modeling of thermochemical convection. *J Geophys Res* 102:22,477–22,495. doi:[10.1029/97JB01353](https://doi.org/10.1029/97JB01353)
- Wen L, Silver P, James D, Kuehnel R (2001) Seismic evidence for a thermo-chemical boundary at the base of the Earth's mantle. *Earth Planet Sci Lett* 189:141–153. doi:[10.1016/S0012-821X\(01\)00365-X](https://doi.org/10.1016/S0012-821X(01)00365-X)